Resistance prediction using CFD at model- and full-scale and comparison with measurements

(article starts on next page)

Research paper

Resistance prediction using CFD at model- and full-scale and comparison with measurements

Rui Lopes [a],*, Arash Eslamdoost [a], Rikard Johansson [b], Seemontini RoyChoudhury [b], Rickard E. Bensow [a], Per Hogström [a], Dmitriy Ponkratov [c]

[a] *Chalmers University of Technology, Department of Mechanics and Maritime Sciences, Gothenburg, Sweden*
[b] *Kongsberg Maritime Hydrodynamic Research Centre, Kongsberg Maritime Sweden AB, Kristinehamn, Sweden*
[c] *Siemens Digital Industries Software, London, United Kingdom*

ARTICLE INFO

ABSTRACT

This study addresses the numerical prediction of the resistance of the Lucy Ashton, a paddle steamer which was used in an experimental campaign in the 1950s, and for which there is available measurement data at both model-scale and full-scale. This case corresponds to unique conditions where jet engines were used in the propulsion of the hull at ship-scale, circumventing the need for a propeller or the ship to be towed by another vessel and thus avoiding interference effects. The computations were carried out for a range of Froude numbers at full-scale, and varying scaling ratios for a constant Froude number. The comparison of the numerical results with the available measurement data shows the simulations to underpredict the resistance for all conditions. The discrepancy observed at full-scale is attributed partially to roughness effects not being included in the computational setup, and due to the even keel configuration of the ship in which the simulations were performed. The ITTC 1978 procedure was applied to the model-scale results, and it was found that the scaled resistance coefficient overpredicts the resistance reported in the experimental campaign and the resistance obtained in the simulations when roughness and air resistance are included in the procedure.

1. Introduction

The design of a marine vessel is composed of different stages, each with their own challenges and importance. Hull and propeller design are two important parts of this process, and not entirely independent of each other. Propeller performance is often estimated in open-water conditions, although in reality the propeller operates in the wake of the ship and in waves. In the same way, one of the important considerations in the design of the hull is minimizing its resistance.

The estimation of the performance of a ship following the 1978 ITTC method (ITTC, 2021) requires data from a resistance test, a self-propulsion test and the characteristics of the propeller. All of the data is obtained at model-scale, with the tests performed at the same Froude number of the full-scale operation. The procedure then provides the full-scale performance, correcting for the difference in the Reynolds number. Another alternative to predict the performance of the ship is through Computational Fluid Dynamics (CFD). In this approach, often done as a complement to experimental tests, computational tools are employed to obtain the required data.

In practice, CFD can be applied directly at full-scale, removing the need to apply any scaling procedure and avoiding the associated

uncertainties in the friction line used or the determination of the form factor (Niklas and Pruszko, 2019; Korkmaz et al., 2021b,a). However, the application of CFD requires thorough validation, which necessitates careful experiments and data for the validation. The challenges in full-scale CFD are many, due to roughness effects and turbulence modelling and the high Reynolds number of the flow, which leads to further demands on the computational requirements, as well as lowering overall grid quality due to the highly stretched cells in the prism layers. Furthermore, data for validation is scarce, due to the higher cost of building a prototype rather than a model, and conditions in sea trials such as currents, wind and waves cannot be as controlled as they are in towing tanks or cavitation tunnels. For these reasons, CFD has not yet gained the same level of confidence at full-scale than it has at model-scale.

In the last few years, bolstered by the available computational resources and the established maturity at model-scale, there has been a growing focus on full-scale CFD. One of the first examples of a full-scale simulation of self-propulsion is given in Castro et al. (2011), although no data was available for validation. Further examples of full-scale

---

simulations are given in Terziev et al. (2019), Sezen et al. (2021), which investigate scaling effects using CFD and in Liu et al. (2021) the full-scale simulation of a free running submarine is addressed. Guidelines for simulations at full-scale have been proposed in Song et al. (2021), Huang et al. (2023). While none of the previous examples address any comparison with full-scale measurement, in Ponkratov and Zegos (2015) a comparison of full-scale self-propulsion CFD results with sea trials for a tanker is given and good agreement between the measurements and the numerical results was observed. A similar exercise was done in Jasak et al. (2019) for a general cargo carrier and a car carrier, including a grid refinement study, with the results showing a good agreement for propeller rotation speed and the speed of the ships. The influence of surface roughness on validation of full-scale simulations is discussed in Mikkelsen and Walther (2020), Quist et al. (2023).

There have been two notable group efforts focused on full-scale simulations. The first was the Lloyd's Register full-scale numerical modelling workshop in 2016 (Ponkratov, 2017), where the community was challenged to compute ship scale simulations of resistance, propeller open water performance, ship self-propulsion and propeller cavitation for a general cargo vessel. The second effort corresponds to the JoRes Joint Industry project, which concluded in 2023. The project has now established a database of six different vessels, for which sea trials have been performed with as much control as possible, and can be used for full-scale validation. CFD workshops for two of the ships were also conducted within the project. The data will be made publicly available in December of 2024.

In spite of the currently ongoing efforts, one gap still lies in the available full-scale data, connected to the propulsion of the ship, as the available full-scale measurements and trials are all done for self-propulsion. Resistance tests cannot be performed as easily as in model-scale conditions, since this would require the ship to not have a propeller installed, meaning that some other form of propulsion must be found. In early experiments performed by Froude in 1874, the H.M.S. Greyhound was towed by an outrigger connected to a larger vessel in order to verify Froude's Law (Crichton, 1989). Some discrepancies were observed at the time, which were attributed to the roughened state of the Greyhound (Denny, 1951). Although towing provides a means for the ship to move without the need for its own propulsion, it introduces different challenges since it becomes impossible to guarantee that there are no interference effects between the two vessels, and also makes maneuvering more difficult.

One unique campaign of measurements was performed in the 1950s, where the propulsion of the ship was achieved through jet engines. In this endeavour, the Lucy Ashton paddle steamer was fitted with four Rolls-Royce jet engines on its hull, as depicted in Fig. 1 which provided a means of propulsion which did not require another vessel to be involved, thus avoiding the problem of interference effects. The experimental campaign was extensive, covering different speeds, four surface finishings, the effect of shaft-appendages and acceleration and retardation runs at full-scale. As part of the project, six models of different scales were also constructed and the resistance was measured at different speeds for each of them. The results of the project were presented in a series of four papers (Denny, 1951; Conn et al., 1953; Lackenby, 1954; Smith, 1955).

The geometry was further used in wind-tunnel testing (Joubert and Matheson, 1970), to assess roughness effects (Smits et al., 1980), and to study turbulence tripping (Smits, 1982). The data from the experiments has also been used in investigations on full-scale resistance estimation (Granville, 1974), on the influence of model size on form factor (García-Gómez, 2000) and addressed in some investigations by the ITTC (ITTC, 1999, 2008). Despite the experimental work, and to the authors best knowledge, no CFD simulations of this vessel have been published so far as seemingly the Lucy Ashton experiments are not well known amongst the community. Considering the available data provided through the experiments, the Lucy Ashton provides a much
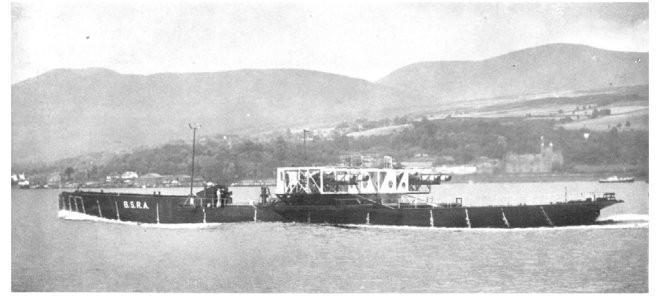

Fig. 1. Lucy Ashton, as modified with the jet engines for the sea trials.
Source: Image adapted from Denny (1951).

valuable and unique opportunity for the prediction of resistance at full-scale. Furthermore, it can be used to also evaluate scaling effects on the resistance, outside of any influence due to propeller-hull interaction.

This work details simulations carried out using the Reynolds-averaged Navier–Stokes equations for the Lucy Ashton at both full-scale and model-scale. The simulations at full-scale consider four different speeds, and the model-scale simulations are performed at a constant Froude number corresponding to one of the conditions ran at full-scale. Although most of the simulations are performed considering the hull to be hydrodynamically smooth, the effect of roughness at full-scale is also considered at one speed, with simulations performed for four different levels of the equivalent sand-grain roughness. Simulations in which the ship is free to heave and pitch are also considered, in order to address the influence of the ship's equilibrium position on the resistance. Finally, the ITTC 1978 procedure is applied to the measured and computational model-scale data, with the scaled resistance being compared to the full-scale values. With this work, the authors address a comparison between numerical results and the experimental measurements, hoping to bring more visibility to this particular geometry which represents a unique opportunity for the growing maturity of full-scale CFD in maritime applications.

The remainder of the paper is organized in the following manner: Section 2 presents the mathematical models used in this work, covering the RANS equations, turbulence model and roughness function used in this work. The numerical setup, including computational domain, boundary conditions and simulated conditions, is described in Section 3. The results for all the simulations are presented and discussed in Section 4, Finally, the conclusions of this work are summarized in Section 5.

2. Mathematical models

All the simulations performed for this study consider the flow of an incompressible Newtonian fluid. The high Reynolds number of the flow and the importance of turbulence imply that the Reynolds-averaged Navier–Stokes are used. Since the flow is unsteady, the Reynolds-average corresponds to an ensemble average. The RANS equations are given by;

$$\frac{\partial U_i}{\partial x_i} = 0, \tag{1}$$

$$\frac{\partial U_i}{\partial t} + \rho U_j \frac{\partial U_i}{\partial x_j} = -\frac{\partial P}{\partial x_i} + \frac{\partial}{\partial x_j}\left[\mu\left(\frac{\partial U_i}{\partial x_j} + \frac{\partial U_j}{\partial x_i}\right)\right] + \frac{\partial \tau_{ij}}{\partial x_j}, \tag{2}$$

in which U_i and U_j are the Cartesian components of the mean velocity, x_i and x_j are the components of the Cartesian coordinate system, P is the mean pressure, ρ is the density of the fluid, μ is the dynamic viscosity and τ_{ij} is the Reynolds stress tensor.

The Reynolds stresses are determined through the eddy viscosity assumption

$$\tau_{ij} = \mu_t\left(\frac{\partial U_i}{\partial x_j} + \frac{\partial U_j}{\partial x_i}\right) - \frac{2}{3}k\delta_{ij}, \tag{3}$$

where μ_t is the eddy viscosity, k is the turbulence kinetic energy and δ_{ij} is the Kronecker delta function.

To calculate the eddy viscosity, the $k - \omega$ Shear Stress Transport (SST) model is used. This means that the solution process deals with two more transport equations, one for k and another for the dissipation variable, ω. These equations can be written as

$$\rho U_j \frac{\partial k}{\partial x_j} = \mu_t S^2 - \rho \beta^* \omega k + \frac{\partial}{\partial x_j}\left[\left(\mu + \sigma_k \mu_t\right)\frac{\partial k}{\partial x_j}\right], \quad (4)$$

$$\rho U_j \frac{\partial \omega}{\partial x_j} = P_\omega - \beta \omega^2 + \frac{\partial}{\partial x_j}\left[\left(\mu + \sigma_\omega \mu_t\right)\frac{\partial \omega}{\partial x_j}\right] + 2\left(1 - F_1\right)\frac{\rho \sigma_{\omega 2}}{\omega}\frac{\partial k}{\partial x_j}\frac{\partial \omega}{\partial x_j}. \quad (5)$$

In these equations, S is the mean strain-rate magnitude, F_1 is a blending function of the model, P_ω is the production term of the ω equation and β, β^*, σ_k, σ_ω and $\sigma_{\omega 2}$ are constants of the model. The formulation of the model is the one given in Menter (1994) with two exceptions. The first corresponds to the production term of the k transport equation, which does not include any limiter. The second difference is in the calculation of the eddy viscosity which includes Durbin's limiter (Durbin, 1996) to prevent high values of μ_t in stagnation regions. With this limiter, the eddy viscosity is given by

$$\mu_t = \rho k \min\left(\frac{1}{\max\left(\omega, \left(S F_2\right)/0.31\right)}, \frac{0.6}{\sqrt{3}S}\right), \quad (6)$$

where F_2 is another blending function of the model.

In some of the simulations carried out in this paper, the modelling of roughness effects is used in conjunction with wall functions the boundary layer treatment. For these conditions the log-law is given by

$$U^+ = \frac{1}{\kappa}\ln\left(y^+\right) + B - \Delta U^+, \quad (7)$$

in which U^+ and y^+ correspond to the velocity and coordinate in the wall normal direction given in wall units, respectively, κ is the von Kármán constant and B is a constant. The roughness function ΔU^+ is the change in the velocity profile caused by the roughness effects, and is given by (Demirel et al., 2017)

$$\Delta U^+ = \begin{cases} 0, & k^+ \leq 3 \\ \frac{1}{\kappa}\ln\left(0.26 k^+\right)^{f(k^+)}, & 3 < k^+ \leq 15 \\ \frac{1}{\kappa}\ln\left(0.26 k^+\right), & 15 < k^+, \end{cases} \quad (8)$$

where

$$f(k^+) = \sin\left(\frac{\frac{\pi}{2}\log\left(\frac{k^+}{3}\right)}{\log(5)}\right). \quad (9)$$

In these equations, k^+ is the dimensionless roughness height, defined as

$$k^+ = \frac{\rho k_s u_\tau}{\mu}, \quad (10)$$

where k_s is the equivalent sand-grain roughness height and u_τ is the friction velocity, calculated as

$$u_\tau = \sqrt{\frac{\tau_w}{\rho}}, \quad (11)$$

with τ_w corresponding to the wall-shear stress.

The multiphase flow is modelled using the Volume of Fluid (VOF) approach (Hirt and Nichols, 1981), which captures the interface between the two phases, air and water. The differential equation for the water volume fraction α is

$$\frac{\partial \alpha}{\partial t} + U_j \frac{\partial \alpha}{\partial x_j} = 0. \quad (12)$$

At each location in the domain, the density and dynamic viscosity are given by

$$\rho = \rho_{water}\alpha + \rho_{air}\left(1 - \alpha\right), \quad (13)$$

$$\mu = \mu_{water}\alpha + \mu_{air}\left(1 - \alpha\right). \quad (14)$$

Table 1
Particulars of the Lucy Ashton.

Characteristic	Symbol	Value
Length between Perpendiculars	L_{pp} [m]	58.1
Breadth	B [m]	6.4
Depth	D [m]	2.18
Block coefficient	C_B	0.685
Prismatic coefficient		0.705
Midship section coefficient	C_M	0.972
Wetted surface area	S [m^2]	416.9
Displaced mass	Δ [kg]	396,240

One potential problem associated with multiphase flow is the smearing of the free-surface, in which the transition between air and water gets spread among several cells. Additionally, the smearing of the free-surface can lead to numerical ventilation, where air flows underneath the hull, naturally influencing the predicted friction resistance. More details can be found in Gray-Stephens et al. (2021), Viola et al. (2012). In order to avoid the smearing of the free-surface on the surface of the hull, a source term S_α is added to the transport equation for the volume fraction of air, defined as

$$S_\alpha = -5\alpha_{air}F_{zone} \quad (15)$$

where F_{zone} is a function that depends on the wall distance and takes values of 0 and 1, in order for the source term to only be active in the vicinity of the hull.

3. Numerical setup

All the simulations in this study were carried out using the commercial CFD software STAR-CCM+ version 2310. The finite volume method is used for the discretization of the transport equations, and their solution is performed using the segregated solver and the SIMPLE algorithm for the pressure-velocity coupling. The time discretization is done using a first order implicit scheme, while second order discretization schemes are used for the convective terms of the continuity, momentum and turbulence equations, and the HRIC scheme (Muzaferija and Peric, 1998) is used for the convection term of the VOF equation.

The vessel considered for the simulations is the Lucy Ashton, a paddle steamer which was built and started its service in 1888. The main particulars of the ship are given in Table 1. For the purpose of the trials carried out in the 1950s, the structure corresponding to the paddle-wheels was removed, and the surface of the hull was cleaned. The geometry of the hull was reproduced in a CAD file based on the drawings available from measurements of the hull during the experimental campaign. The structure supporting the jet engines was not included in the modelling, and the junction of the hull and the rudder at the keel was smoothed out in order to avoid problems when generating the grid.

The computational domain is a box with a length of $6L_{pp}$, width of $2L_{pp}$ and height of $2L_{pp}$. The ship is positioned in the computational domain such that the inlet is located approximately $2L_{pp}$ from the bow and the outlet is $3L_{pp}$ away from the aft. A symmetry plane is placed at the centreline of the ship, and the bottom boundary is $0.5L_{pp}$ away from the keel. The origin of the coordinate system is located at the aft perpendicular, along the centreline and keel of the ship.

The simulations at full-scale are performed for four different speeds, ranging from $V_\infty = 3.1$ m/s up to $V_\infty = 6.2$ m/s. This corresponds to Froude numbers from $Fr = 0.13$ to 0.26, and Reynolds numbers from 1.6×10^8 to 3.1×10^8. The simulations at model-scale are done for a constant Froude number of $Fr = 0.17$, which is also one of the conditions done at full-scale. Six model scales are considered, for scaling ratios λ ranging from 6.4 to 21.2. The Reynolds number at model-scale ranges from 1.9×10^6 up to 1.2×10^7. While all conditions are simulated for fixed draught and at even keel, calculations where the ship is free to heave and pitch are also performed at full-scale

Table 2
Details about the grids generated for the full-scale simulations for the lowest Froude number.

Grid designation	Free-surface		Double-body	
	#S	#V	#S	#V
5	84,917	4.0M	30,879	1.0M
4	132,865	7.5M	47,380	2.0M
3	184,193	12.4M	65,129	3.2M
2	251,960	19.4M	89,377	5.1M
1	326,400	28.8M	114,431	7.4M

Table 3
Details about the grids generated for the model-scale simulations for the highest scaling ratio.

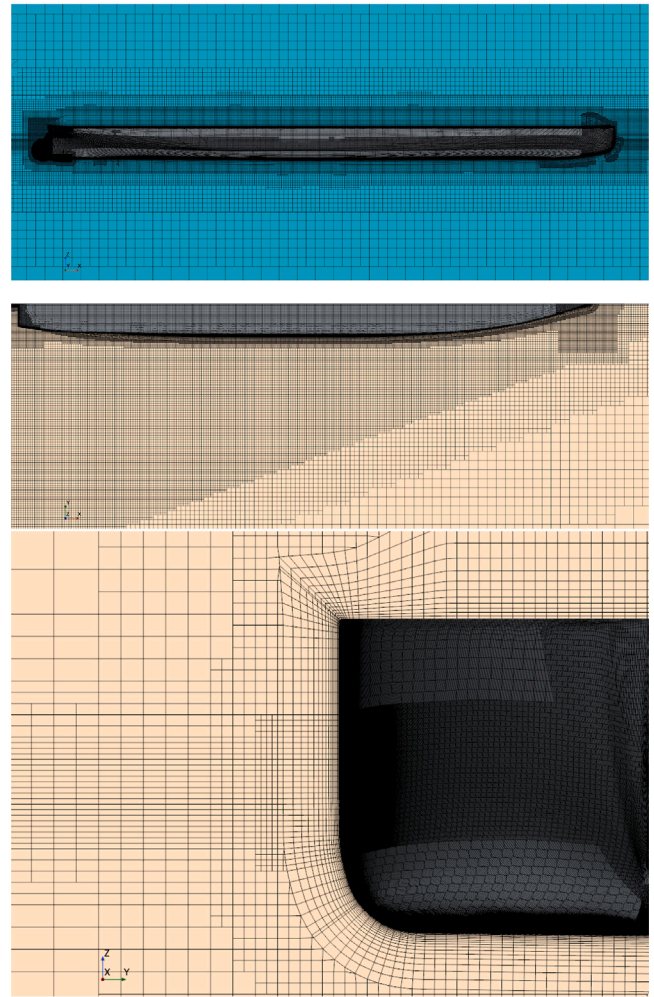| Grid designation	Free-surface		Double-body	
	#S	#V	#S	#V
5			30,949	1.5M
4			46,163	2.9M
3	182,783	16.3M	62,798	4.6M
2			85,735	7.3M
1			110,347	10.7M

Fig. 2. Side view (top), top view (middle) and front view (bottom) of the coarsest grid for the full-scale simulation with the free-surface.

for $Fr = 0.17$. This same scenario is used to study the influence of roughness modelling for four different equivalent sand-grain roughness heights, for the roughness function given in Demirel et al. (2017).

The grids for the simulations are generated using the trimmer and the prism layer meshers. For the full-scale conditions, the grids are generated such that wall functions can be used. For the model-scale simulations, the distance of the near-wall cell size is set so that $y^+_{max} < 1$, such that wall functions are not used and the boundary-layer is resolved.

A set of five grids is generated for each scale in order to obtain an estimate of the numerical uncertainty. The unstructured topology of the grids implies that it is impossible to generate the grids so that they are geometrically similar. Nonetheless, all parameters are set so that they are as similar as possible. It is noted that for the full-scale setup, the size of the near wall cell also decreases with grid refinement, instead of staying constant. In order to guarantee that wall functions are applicable for all five grids, the coarsest grid is designed so that $y^+ \approx 100$. Furthermore, different grids are generated for each Froude number, due to the change in the Reynolds number affecting y^+_{min}.

For all conditions, simulations on a double-body setup are carried out as well. The grids for these simulations are generated from the grids for the free-surface simulations, by simply changing the location of the top boundary to the undisturbed free-surface level, and removing all refinement zones set to capture the free-surface, leading to a much lower cell count. This means that each condition (Froude number and scale) has its own grid set, corresponding to a total of 76 grids.

Tables 2 and 3 present the number of cell faces on the ship, #S, and the total number of volume cells, #V, for the full-scale and model-scale grids, respectively. The details corresponding to the full-scale grids are those of the grids generated for the lowest speed, whereas the values given for the model-scale grids are those for the smallest model ($\lambda = 21.2$). Although there are some small changes for the grids at different speeds or scales, the numbers given in the tables are representative of all cases. The grid topology is illustrated in Figs. 2 and 3 for the grids with the free-surface and the double-body setup, respectively.

The generation of sets of five grids is motivated by the estimation of the numerical uncertainty of the resistance. The method employed (Eça and Hoekstra, 2014) relies on writing the discretization error e as

$$e \approx \phi_i - \phi_0 = \alpha h_i^p, \qquad (16)$$

where ϕ_i is the value of a given quantity of interest in grid i, ϕ_0 is the estimate of the exact solution of the mathematical model for that same quantity, α is the error constant, p is the order of grid convergence and h_i is a measure of the grid refinement level. The solutions from the

five grids are used to solve Eq. (16) in the least-squares sense, with the estimated uncertainty depending on the quality of the fit and on the change in the solution on all grids.

A proper estimation of the numerical uncertainty based on grid refinement studies requires the assumption that the discretization error is the dominant contribution to the numerical error, meaning that the remaining sources of error must be minimized. In the case of unsteady simulations, the numerical error also has contributions for the round-off error, iterative error, and statistical error. The round-off error is caused by the limited precision in which computers operate, and is minimized by using the double-precision version of STAR-CCM+. The iterative error is due to the linearization of the discretized equations and the iterative procedures used in the solution of the linear system of equations, and is minimized by converging the solution sufficiently within each time-step. Finally, the statistical error is a consequence of the initial condition with which the iterative procedure is started, and is reduced by running the simulation for enough time so that the influence of the initial condition on the solution is negligible.

The grid refinement studies are not carried out for all settings. Regarding the double-body setup, the simulations are always carried out on the five grids due to the much lower cost of these simulations owning to the lower cell count and steady approach. For the simulations with the free-surface, the grid refinement study is only performed for the full-scale conditions with fixed draught and no roughness modelling. For the remaining cases, only the intermediate
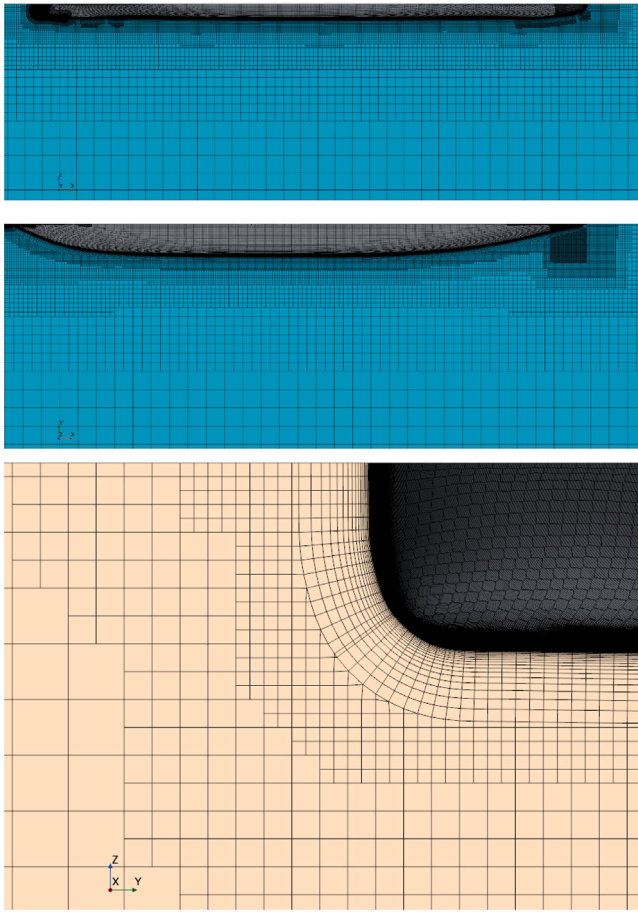
Fig. 3. Side view (top), top view (middle) and front view (bottom) of the coarsest grid for the full-scale simulation with the double-body setup.

Table 4
Summary of the grids used for each condition, given in terms of scaling ratio λ, Froude number and Reynolds number.

λ	Fr	Re	Free-surface	Double body	Roughness	Motion
1.0	0.13	1.6×10^8	Grid set	Grid set	No	No
1.0	0.17	2.1×10^8	Grid set	Grid set	Yes	Yes
1.0	0.22	2.6×10^8	Grid set	Grid set	No	No
1.0	0.26	3.1×10^8	Grid set	Grid set	No	No
6.35	0.17	1.2×10^7	Single grid	Grid set	No	No
7.94	0.17	8.4×10^6	Single grid	Grid set	No	No
9.53	0.17	6.4×10^6	Single grid	Grid set	No	No
11.91	0.17	4.6×10^6	Single grid	Grid set	No	No
15.88	0.17	3.0×10^7	Single grid	Grid set	No	No
21.17	0.17	1.9×10^7	Single grid	Grid set	No	No

C_p, given by

$$C_f = \frac{\tau_w}{\frac{1}{2}\rho V_\infty^2}, \tag{18}$$

$$C_p = \frac{P - P_{ref} - g\rho z}{\frac{1}{2}\rho V_\infty^2}, \tag{19}$$

where τ_w is the wall shear stress, g is the acceleration of gravity, P_{Ref} is the reference pressure and z is the vertical position.

4. Results

4.1. Numerical uncertainty

The discussion of the results starts by addressing the estimated numerical uncertainty. The convergence of the resistance coefficient is shown in Fig. 4 for the simulations at full-scale with the double-body setup and with the free-surface for different Froude numbers. A similar analysis is conducted at model-scale for the double-body setup, and shown in Fig. 5. In these figures, r_i/r_1 corresponds to the ratio between the refinement level of each grid (r_i) relative to the finest grid (r_1). This means that $r_i/r_1 = 1$ corresponds to the finest grid. Regarding the full-scale conditions, the comparison between the free-surface and double-body setup shows that lower numerical uncertainty is obtained for the double-body setup. For this setup, the increase of the Froude number appears to lead to a general increase of the numerical uncertainty, whereas for the simulations with the free-surface no clear trend is observed. The uncertainty on the finest grid goes up to 2% for the simulations with the free-surface, and up to 0.8% for the simulations with the double-body approach.

When looking at the model-scale results the main trend observed is that the numerical uncertainty tends to increase as the scaling ratio decreases, or equivalently, as the Reynolds number increases. However, the uncertainty obtained for the lowest scaling ratio is considerably higher than that obtained for the same Froude number at full-scale. This discrepancy is attributed to the different strategies to handle the boundary layer, as wall functions are used at full-scale, while the boundary layer is resolved at model-scale.

The previous comments pertain only to the total resistance of the ship. When considering solely the friction component of the resistance for the full-scale simulations, its numerical uncertainty does not follow any trend, similarly to the total resistance, and ranging from 1.0% at $Fr = 0.13$ up to 1.8% at $Fr = 0.26$ when the free-surface is included in the simulations. On the other hand, the relative uncertainty of the pressure resistance decreases with the increase of the Froude number, although its absolute value does increase as Fr is increased. In the case of the full-scale simulations with the double-body setup, no trend is observed in the friction component, while the pressure resistance exhibits a slight increase with the increase of the Froude number. Finally, for the model-scale simulations with the double-body approach, the uncertainty of the friction resistance matches closely with that observed for the total resistance, whereas the uncertainty of the pressure resistance does not show any clear trend with the change in the Reynolds number.

grid of the set (grid 3) is used.

A summary of the conditions considered in this study is given in Table 4. A total of 82 simulations were carried out, with 32 of those including the free-surface, and 50 with the double-body setup. The simulations at full-scale and $Fr = 0.17$ with roughness or free heave and pitch motions were only carried out for the free-surface setup and a single grid. For the same conditions ($Fr = 0.17$ and $\lambda = 1.0$) the simulations without roughness and with the fixed ship position were done for the entire grid set. The simulations with the free-surface ran for an average of 20,000 timesteps. Intel(R) Xeon(R) Gold 6338 CPUs were used for the simulations, with a total of 320 cores per simulation for most of the grids. For this setup, the grid sets for the free-surface simulations took around 12 days each, whereas the single grid computations took around 3 days. The computational time of the simulations of the double-body setup was a negligible fraction of the total time, due to the lower number of cells in the grids and the steady approach.

The resistance coefficient C_T is the main quantity of interest in this work. It is defined as

$$C_T = \frac{R}{0.5\rho V_\infty^2 S}, \tag{17}$$

where R is the resistance of the ship, V_∞ is the undisturbed flow velocity and S is the wetted surface area. The decomposition of the resistance coefficient into the corresponding friction and pressure contributions is considered as well.

We also consider local quantities such as the elevation of the free-surface ξ, the skin-friction coefficient C_f and the pressure coefficient
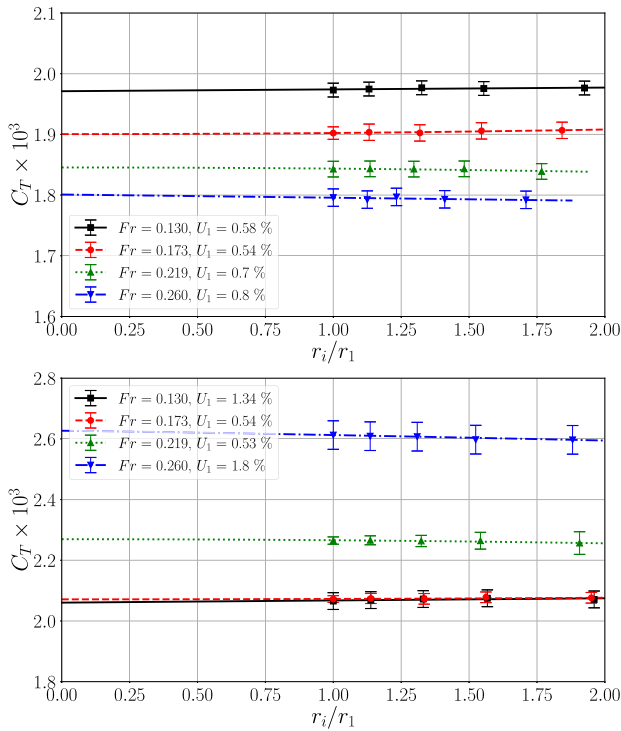
Fig. 4. Convergence of the resistance coefficient with grid refinement at full-scale for the simulations performed with the double-body setup (top) and with the free-surface (bottom).
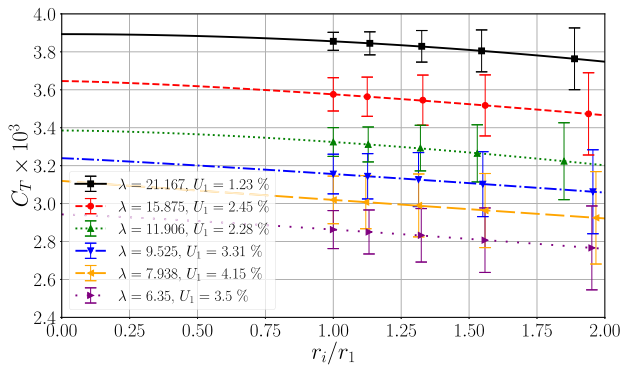

Fig. 5. Convergence of the resistance coefficient with grid refinement at model-scale for the simulations performed with the double-body setup.

4.2. Free-surface smearing

As previously stated, a source term was added to the equation for the volume fraction in the simulations. In order to assess the influence of the source term, we compare simulations with and without source for different conditions. Fig. 6 illustrates the volume fraction on the surface of the hull for the full-scale simulations performed at the lowest Froude number obtained both with and without the source term. This condition is the one that is the least affected by the smearing of the free-surface, which only occurs in a small region located near the bow of the ship. The use of the source term reduces the smearing in this zone, and more importantly, it does not seem to have any significant effect in the remainder of the hull, where the interface between the two regions is already sharp, thus showing that the source term does not appear to have negative effects on the simulation.

The practical benefits of the source term at full-scale are illustrated in Fig. 7 which depicts the volume fraction on the surface of the ship
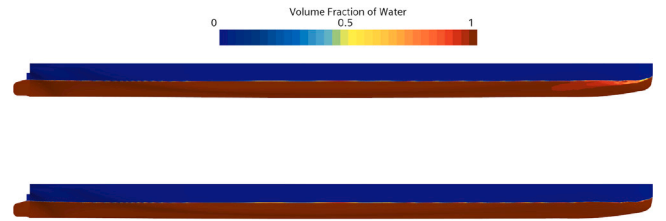

Fig. 6. Volume fraction of water on the surface of the hull for the simulations performed at full-scale and the lowest Froude number without (top) and with (bottom) the source term to the volume fraction equation.
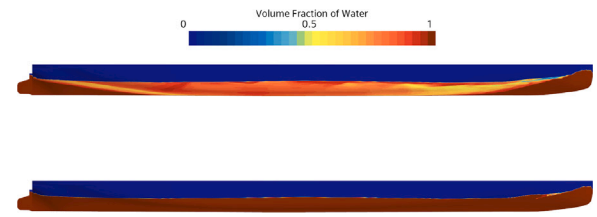

Fig. 7. Volume fraction of water on the surface of the hull for the simulations performed at full-scale and the highest Froude number without (top) and with (bottom) the source term to the volume fraction equation.

for the highest Froude number. For these conditions there is a clear smearing of the free-surface if the source term is not used, starting shortly after the bow and covering a large part of the hull up to the aft. It is also observed that the smearing mostly occurs for volume fraction values in the range $0.5 < \alpha < 1.0$, and that for the most part, the position of the interface on the surface of the hull can still be easily distinguished. The use of the source term remedies this situation, and leads to a much sharper interface. Some smearing is still observed in a small region close to the bow, although the size of this region is much smaller than when the source term is not used. One direct consequence of the smearing of the free-surface is that the resistance of the hull is lower than it should be, due to the decreased friction resistance caused by the incorrect fluid viscosity in the part of the hull where the free-surface is smeared. Therefore the use of the source term to maintain the sharp interface will lead to higher resistance. In the case of the lowest Froude number, since the free-surface is barely changed, the increase is marginal. On the other hand, for the highest Froude number where strong smearing is observed, the resistance increases by 4.9% due to the application of the source term.

An important aspect is that the smearing of the free-surface is not limited to the full-scale conditions, and is also observed for the model-scale simulations. This is shown in Fig. 8, which displays the volume fraction of water on the surface of the hull for the smallest scale considered. As before, results with and without the source term are shown. The smearing at model-scale is more pronounced than it was at full-scale, despite the Froude number for the model-scale conditions being lower than the one corresponding to the simulations previously described in Fig. 7. The stronger smearing observed at model-scale is attributed to the different approach to handle the boundary-layer and corresponding grid requirements. At model-scale, the mesh is generated so that the boundary-layer is resolved, whereas at full-scale wall functions are used instead. As it was the case at full-scale, the use of the source term remedies the situation, leading to a sharper interface.

4.3. Comparison with experimental measurements

One of the main advantages of this particular geometry is the existence of measurements at model-scale and full-scale. In Fig. 9 the resistance coefficient obtained at full-scale with the two numerical approaches is compared with that from the experiments. The scatter
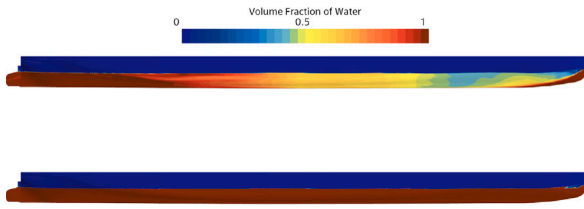
Fig. 8. Volume fraction of water on the surface of the hull for the simulations performed at model-scale ($\lambda = 21.2$) without (top) and with (bottom) the source term to the volume fraction equation.
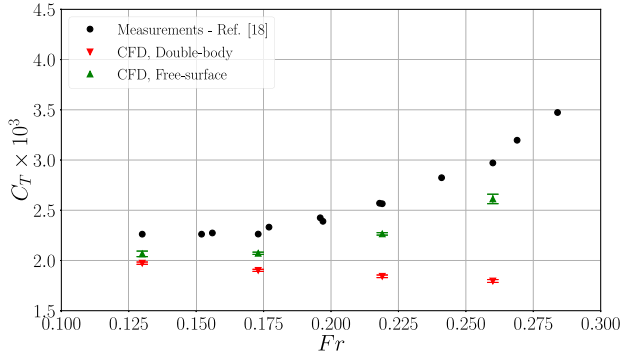
Table 5
Equivalent sand-grain roughness height k_s settings and corresponding dimensionless average roughness k^+.

k_s [μm]	k^+
50	5.7
70	8.1
90	10.7
109	13.2

Fig. 9. Resistance coefficient at full-scale obtained with the double-body approach and the free-surface for varying Froude number and comparison with available experimental data.
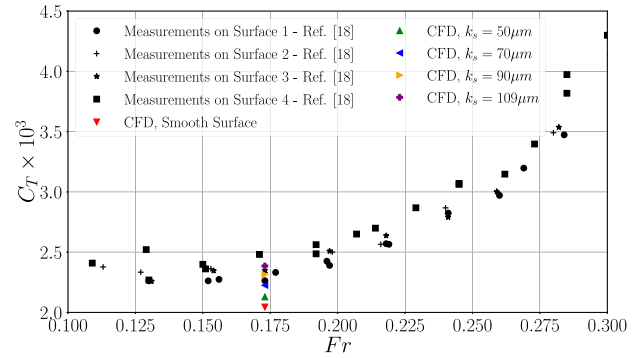

Fig. 10. Resistance coefficient at full-scale obtained with the free-surface for varying equivalent sand-grain roughness heights and comparison with available experimental data.

in the measurements is caused by the different surfaces and paints that were tested, which are not distinguished here. Nonetheless, they are useful as an indication of the effect of roughness observed in the measurements, as well as the measurement uncertainty. The experimental results were corrected to a standard temperature and displacement, as well as for the wind and air resistance and effect of the rudder, according to the best practices at the time. Details on the corrections are detailed in Conn et al. (1953). The computational results underpredict the resistance of the Lucy Ashton, with the discrepancy becoming larger for higher speeds. This is not a surprising result, as the numerical results do not account for any roughness effects, whereas the experimental results with the different paints show this to be an important effect, and the discussion about the roughness measurements in Conn et al. (1953) indicates that the smoothest condition does not correspond to a hydrodynamically smooth surface. When comparing both numerical setups, their mismatch grows as the Froude number increases, due to the increasing dominance of the wave-making resistance in the total resistance. As the simulations with the double-body setup cannot capture the wave-making resistance, the pressure resistance has only a slight increase as the Froude number grows. Consequently, the resistance coefficient decreases slightly with the increase of the Froude number. On the other hand, the simulations with the free-surface have a higher increase of the pressure resistance, thus leading to the increase of C_T with Fr. It is also noted that the friction resistance obtained in the double-body setup is slightly lower than the one obtained when the free-surface is included in the setup.

The reasons for the underprediction of the resistance can be related to the lack of roughness effects, which will affect the friction resistance, and also the fixed setup for the ship, which does not allow for it to heave and pitch. The influence of these aspects on the resistance is considered separately. For a single Froude number ($Fr = 0.173$) at full-scale, four different equivalent sand-grain roughness heights are tested, ranging from 50 μm to 109 μm. These values were selected in order to cover dimensionless average roughness heights of $k^+ = 5.7$ to $k^+ = 13.2$. The details of the four roughness conditions are given in Table 5.

The results for the variation of roughness are given in Fig. 10. An estimation of the equivalent sand-grain roughness based on the roughness allowance is given in Conn et al. (1953). This estimate ranges from 58 μm up to 98 μm depending on the surface finishing, which is a smaller range than the variation considered in the simulations. As is evident, the increase of the roughness height leads to an increase in C_T, mainly due to the increase in the friction resistance. The effect of the variation of k_s appears to be smaller in the numerical predictions than in the measurement data, as the change in C_T is similar, but the change in k_s was larger in the CFD results. Even with the inclusion of roughness effects, the resistance coefficient is still underestimated in the CFD, when comparing to an experimental condition with a similar k_s.

To study the influence of heave and pitch on the ship resistance, the two degrees of freedom were incorporated in the simulation using the Equilibrium model of the Dynamic Fluid Body Interaction capability in STAR-CCM+. The results are depicted in Fig. 11, which compares the resistance coefficient of the ship obtained in the measurements with the results from three simulations. Two of these correspond to hydrodynamically smooth surfaces, one with the position of the ship fixed, and another where the ship is free to heave and pitch. As a final comparison, a third simulation is also included, where the equivalent sand-grain roughness height was set to $k = 58$ μm, and the ship is free to heave and pitch. In this figure, only the smoothest surface conditions from the measurements is displayed. Having the ship free to heave and pitch leads to an increase of wetted surface area and corresponding increase of the resistance. When this effect is combined with the application of the rough surface, a good match in the resistance is observed between the numerical simulation and the experimental measurements for the Froude number considered.

Besides the full-scale conditions, we also consider the model-scale simulations. Fig. 12 illustrates the resistance coefficient obtained for the model-scale simulations using the double-body setup and the free-surface, as well as the results from the measurements, for varying scaling ratio. In all conditions, the simulations with the free-surface lead to a larger C_T than the double-body simulations. When comparing the friction and pressure components individually, it was observed that the friction resistance between the two setups was nearly identical,
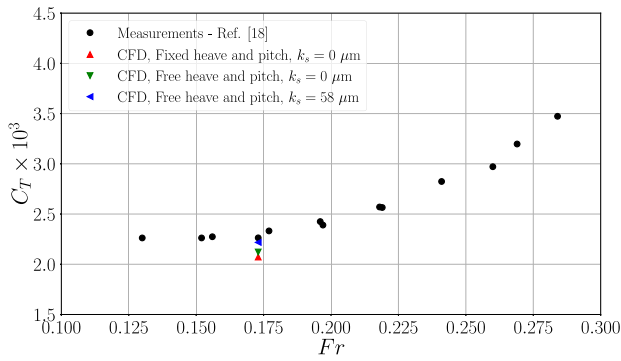
Fig. 11. Resistance coefficient at full-scale obtained with the free-surface and with free heave and pitch, for hydrodynamically smooth and rough surfaces and comparison with available experimental data.
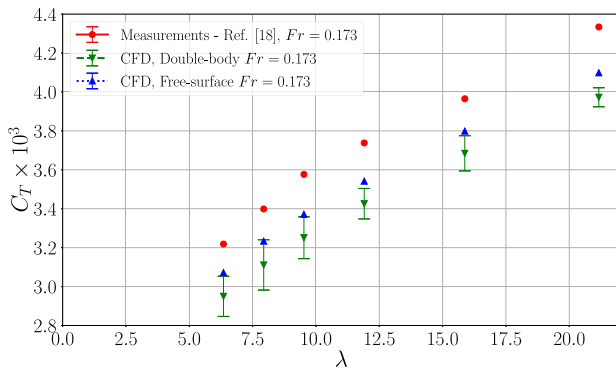

Fig. 12. Resistance coefficient at model-scale for varying scaling ratio and $Fr = 0.173$ obtained with the double-body approach and the free-surface and comparison with available experimental data.

with the difference in C_T arising mainly from the pressure forces, specifically from the wave making resistance. As was the case for the full-scale simulations, the resistance coefficient is again underpredicted for all scaling ratios considered. While at full-scale this was partially attributed to the surface roughness, it seems unlikely for this to be the case at model-scale. It is also worth noting that the highest scaling ratio corresponds to a Reynolds number of 2.1×10^6, which could suggest the flow to be partially laminar. However, the measurement data shown in Fig. 12 corresponds to the runs when the flow was tripped. Furthermore, if the discrepancy was due to laminar effects, then the CFD results would tend to overpredict the resistance instead, since no transition model was used in the simulations and the flow is modelled as being fully turbulent. The description of the measurements in Conn et al. (1953) does not provide sufficient information regarding the experimental setup in order to understand whether the models were also free to heave and pitch, which stands as another cause for the mismatch. However, the issue is not further explored here, as that there are more modern and well documented model-scale experiments for different geometries.

4.4. Comparison of local quantities

In Fig. 13, the transversal C_f distributions at different longitudinal positions are given for the different Froude numbers calculated at full-scale. The longitudinal direction is given by x whereas y corresponds to the transversal direction. The effect of the Reynolds number of the flow is clearly visible on the skin-friction coefficient, with the higher Reynolds number conditions exhibiting lower C_f. Some trends in the evolution of C_f are common for all conditions, with a decrease of C_f from the centreline up to $y/L_{pp} = 0.01$ for the distributions at $x/L_{pp} =$
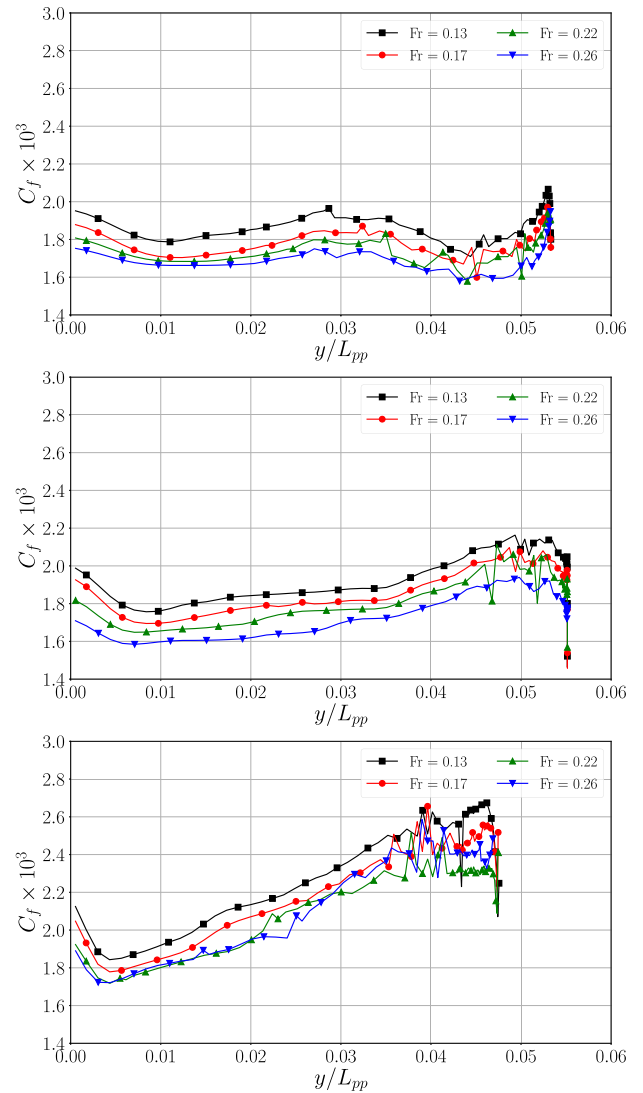

Fig. 13. Skin-friction coefficient distributions at $0.25L_{pp}$ (top), $0.5L_{pp}$ (middle) and $0.75L_{pp}$ (bottom) for the full-scale simulations with the free-surface and varying Froude number.

0.25 and $x/L_{pp} = 0.5$, and up to $y/L_{pp} = 0.005$ for the distribution at $x/L_{pp} = 0.75$. This is then followed by a steady increase of C_f which varies depending on the longitudinal position. At $x/L_{pp} = 0.25$ the increase of C_f is not significant, attaining the maximum value exhibited at the centreline. For the distributions at $x/L_{pp} = 0.5$ and $x/L_{pp} = 0.75$ the increase of C_f is more pronounced, going beyond the value observed at the centreline.

In this region of increasing C_f, some oscillations in the skin-friction distribution are observed, as a consequence of the effects of the free-surface on the flow, and the unstructured grid topology. It should be mentioned that the data was obtained directly at the cell centres, which also results in a non-smooth behaviour that exhibits changes between each condition since different grids were generated for each Froude number. The C_f distribution on the fore part of the wetted surface is displayed in Fig. 14 for $Fr = 0.17$, exemplifying the behaviour. Towards the highest range of y/L_{pp} the skin-friction coefficient decreases sharply, as the free-surface and non-wetted surface are reached.

Fig. 15 shows the pressure coefficient on the surface of the hull for the full-scale simulations, at the three longitudinal positions considered previously. In the distributions at $x/L_{pp} = 0.25$ and $x/L_{pp} = 0.75$, the pressure coefficient decreases with the increase of the Froude number.
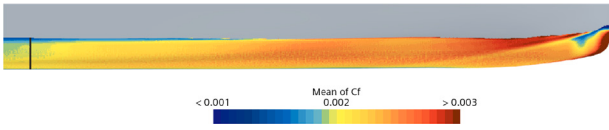
Fig. 14. Skin-friction coefficient distribution on the fore part of the wetted surface for the full-scale simulations with the free-surface and $Fr = 0.17$. The black solid line indicates the mid-ship position, $x = 0.5L_{pp}$.
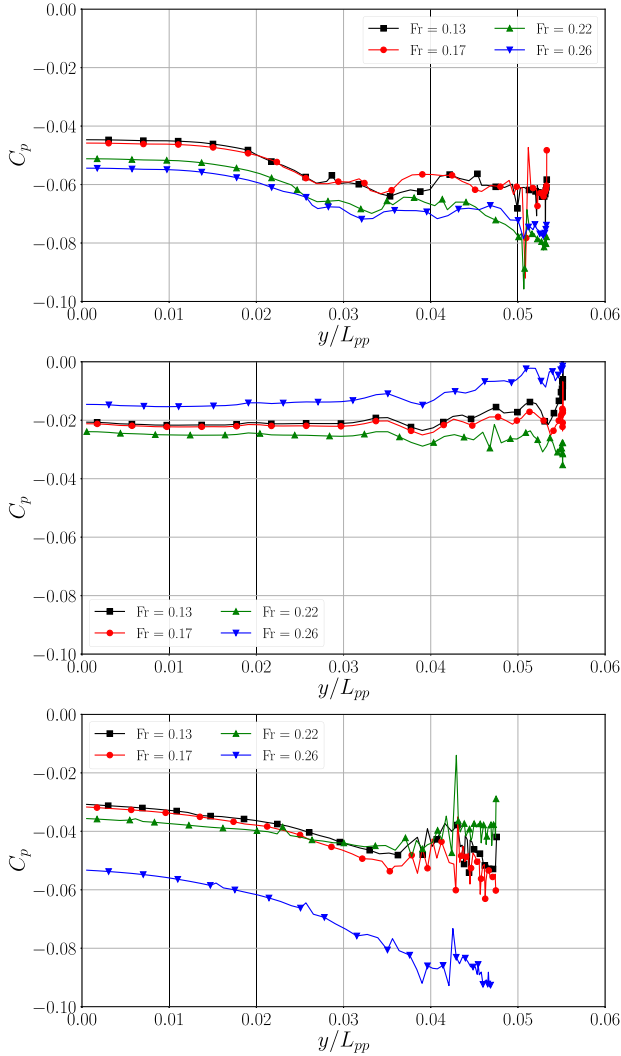

Fig. 15. Pressure coefficient distribution at $0.25L_{pp}$ (top), $0.5L_{pp}$ (middle) and $0.75L_{pp}$ (bottom) for the full-scale simulations with the free-surface and varying Froude number.
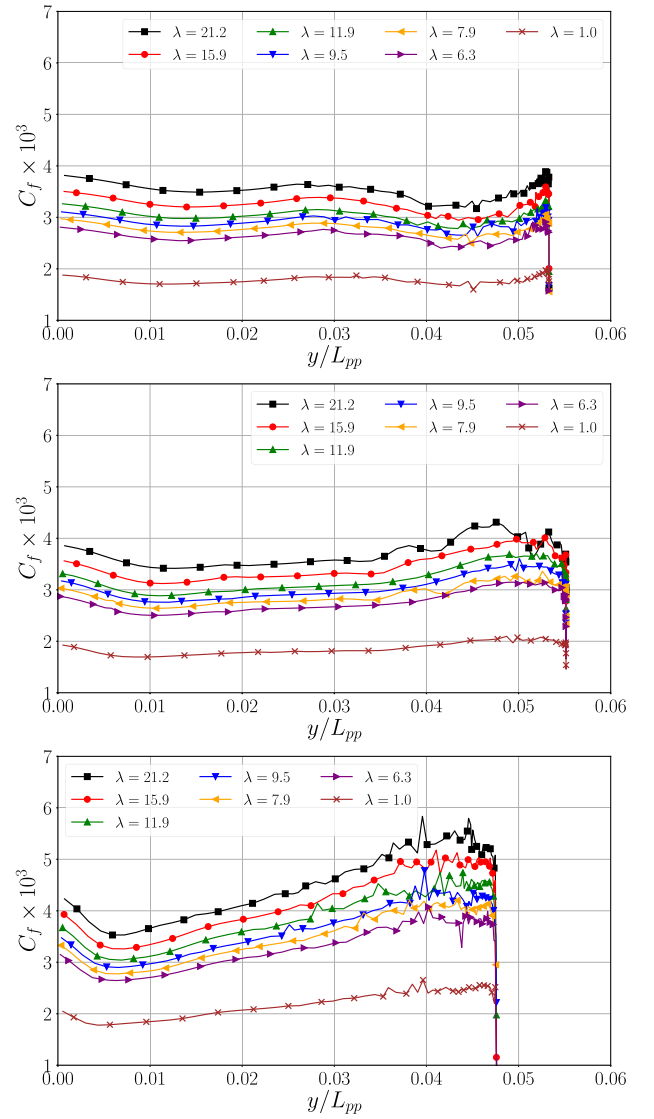

Fig. 16. Skin-friction coefficient distribution at $0.25L_{pp}$ (top), $0.5L_{pp}$ (middle) and $0.75L_{pp}$ (bottom) for the model-scale simulations at $Fr = 0.17$ and varying scaling ratio.

Furthermore, at these positions, the C_p distributions have their maximum at the centreline, with the pressure coefficient decreasing when moving away from it. These trends are not observed at $x/L_{pp} = 0.5$, which shows the two highest Froude numbers exhibiting both the lowest and highest pressure coefficient. Furthermore, at this longitudinal position, the pressure coefficient does not exhibit large changes as one moves in the lateral direction. Finally, at all positions, and similarly to that observed for the C_f distributions, large oscillations are observed in C_p in the area furthest away from the centreline.

A comparison of C_f and C_p for varying scaling ratios and $Fr = 0.17$ is illustrated in Figs. 16 and 17, respectively. The evolution of C_f follows that described for the full-scale condition, with the solutions corresponding to the largest λ exhibiting the highest C_f, as a consequence of the lower Reynolds number. Some oscillations in the

region of $y/L_{pp} = 0.05$ are also observed. With regards to the pressure coefficient the solutions are almost graphically identical, with the main differences coming from the previously mentioned oscillations which are more predominant away from the centreline.

Fig. 18 presents the velocity profile obtained in the full-scale simulations at $x/L_{pp} = 0.49$ as a function of the wall distance d. In these figures, U is the longitudinal velocity and V_∞ the velocity at the undisturbed far-field. The profiles obtained for the four different conditions exhibit only slight changes, with a nearly constant boundary layer thickness. The velocity obtained at the points closest to the wall corresponds to around half of the undisturbed flow velocity, due to the use of wall functions. A similar comparison is performed in Fig. 19 for different scales at a constant Froude number. Here the main change between each condition is the Reynolds number, which impacts strongly the velocity profile. The simulations performed at model-scale exhibit a much more detailed velocity profile, since wall functions were not used. The decrease of the Reynolds number leads to a thicker boundary layer and lower velocity gradient near the wall, with the
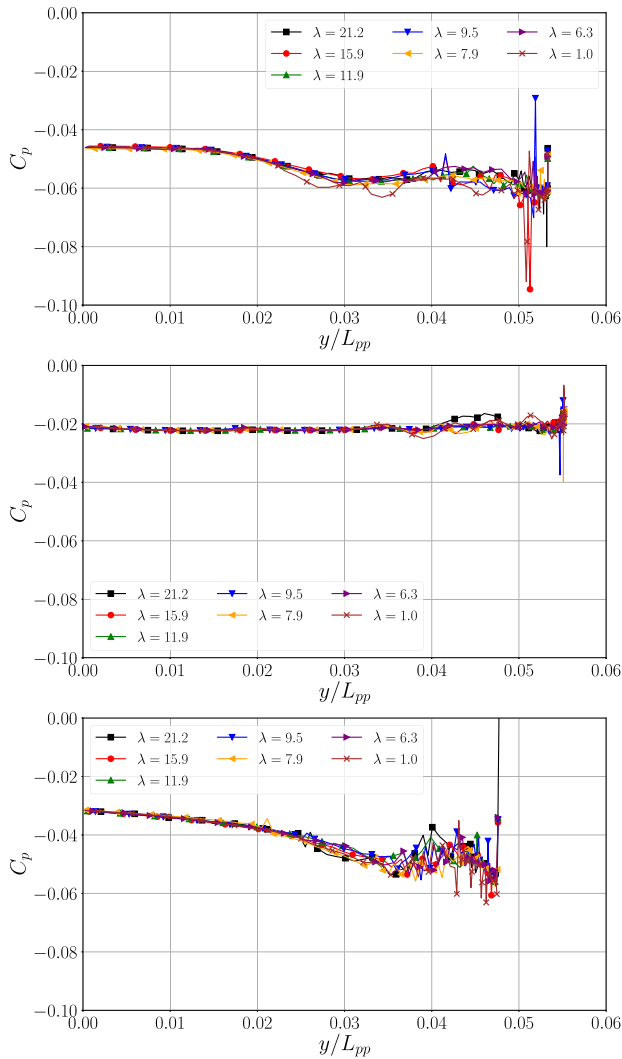
Fig. 17. Skin-friction coefficient distribution at $0.25L_{pp}$ (top), $0.5L_{pp}$ (middle) and $0.75L_{pp}$ (bottom) for the model-scale simulations at $Fr = 0.17$ and varying scaling ratio.
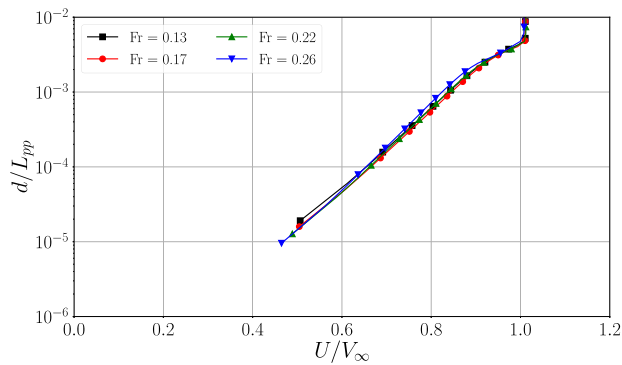

Fig. 18. Velocity profile obtained at full-scale on the symmetry plane at $x/L_{pp} = 0.49$ for varying Froude number.

Fig. 19. Velocity profile obtained on the symmetry plane at $x/L_{pp} = 0.49$ and at $Fr = 0.17$ for varying scaling ratio.

number has a negligible effect on the behaviour of the free-surface for this case, being mostly driven by the Froude number. The only notable exception to this occurs near the aft of the ship and on the boundary layer, where some differences are observed between each scale. These are highlighted in Fig. 21.

4.5. Resistance scaling with the ITTC 78 procedure

As a final step in the analysis of the results, and considering that there are both computational results and available measurements at different scales, we apply the ITTC 78 scaling procedure to the model-scale data and compare it to the corresponding full-scale data. The use of the ITTC 78 procedure requires data at model-scale to calculate both the form factor, $(1 + k)$, and to estimate the wave-making resistance. Considering the work developed during this study, we have both numerical and experimental data at model-scale, which enables several possibilities in the application of the procedure. Five different scenarios are considered, summarized in Table 6 and detailed below:

- In the first scenario (case 1), we rely exclusively on data from the experiments to obtain the form factor and the wave-making resistance. The former is obtained from the measurements using Prohaska's method. For each of the different scales, the calculation of the form factor relies only on the data of that scale.

- In the second scenario (case 2), the form factor is determined from the double-body simulations, but the resistance coefficient of the experiments is still used to obtain the wave-making resistance. As in the first scenario, the calculation of the form factor for a given scale only uses data obtained for that scale.
- In the third approach (case 3), two different form factors are considered, one at model-scale and another at full-scale, and both are obtained from the double-body simulations. The calculation of the wave resistance of the model relies on the experimental resistance coefficient, and on the model-scale form factor. The resistance coefficient of the ship then relies on the full-scale form factor.
- The four and fifth approaches (cases 4 and 5) are similar to the second and third, respectively, with the only difference being that the determination of the wave making resistance relies on the results from the simulation performed at model-scale with the free-surface.

The estimation of the full-scale resistance coefficient according to the ITTC 78 procedure also includes contributions from roughness, in the form of the roughness and correlation allowance, and the effect of air resistance. In the case of the first scenario, where only data from the experiments is used, the comparison should be made against the full-scale measured data. Due to this, the roughness and air resistance

combined effect causing the increase of C_f discussed before.

The elevation of the free-surface at three longitudinal positions is considered in Fig. 20 for varying scaling ratio at a constant Froude number. The results show that the free-surface elevations at the different Froude numbers tend to a single line. This illustrates that the Reynolds
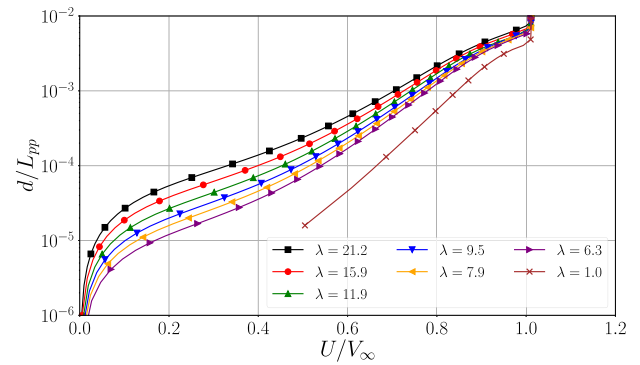
Table 6

Summary of the five cases considered in the application of the ITTC 78 procedure in terms of the source of the model scale resistance, the calculation of the form factor and its dependence on scale.

Case	Model scale resistance	Form factor calculation	Form factor scale independent
1	Experimental	Experimental	Yes
2	Experimental	CFD	Yes
3	Experimental	CFD	No
4	CFD	CFD	Yes
5	CFD	CFD	No

Fig. 21. Elevation of the free surface near the boundary layer at $0.75L_{pp}$ for the model-scale simulations at $Fr = 0.17$ and varying scaling ratio.

Fig. 22. Comparison of the form factor obtained using Prohaska's method on the experimental data and from the double-body simulations for varying scaling ratio.
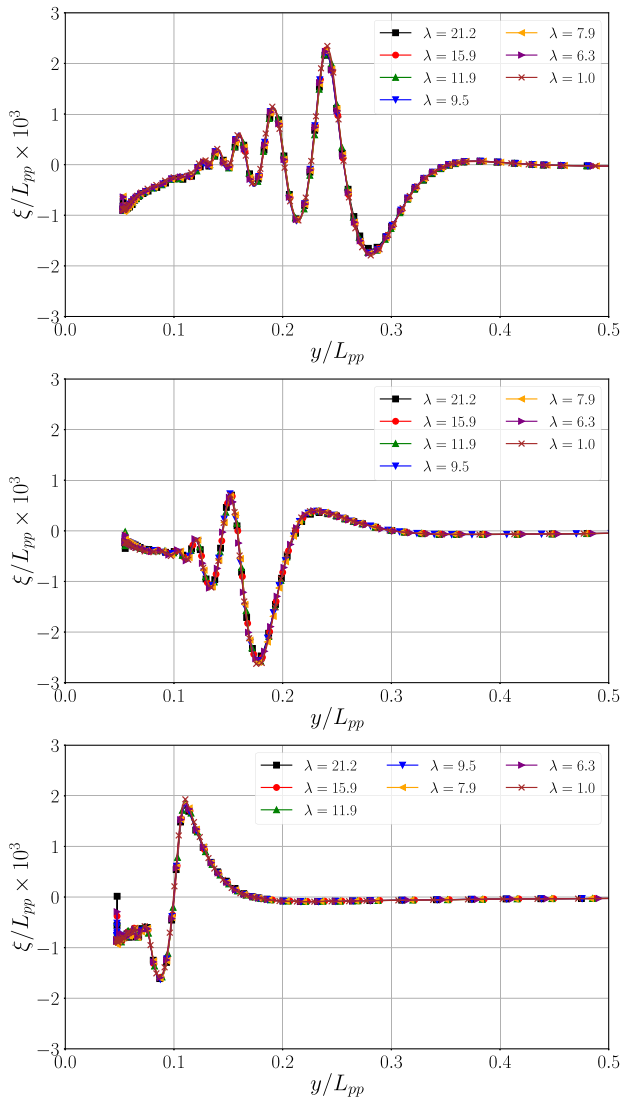
Fig. 20. Elevation of the free surface at $0.25L_{pp}$ (top), $0.5L_{pp}$ (middle) and $0.75L_{pp}$ (bottom) for the model-scale simulations at $Fr = 0.17$ and varying scaling ratio.

effects should be included in the scaling procedure. However, in the fourth and fifth cases, only numerical data is used, and therefore the comparison should be done against the full-scale numerical simulations with the free-surface, which do not include the superstructure and in which the hull was considered as smooth. For these two cases, roughness and air resistance effects should not be accounted for. To accommodate a fair comparison for all cases, the scaling procedure is applied both with and without the roughness and air resistance contributions.

Fig. 22 compares the form factor obtained from the measurements and from the double-body simulations for each scale. It is observed that there are large variations in the form factor with the scaling ratio when
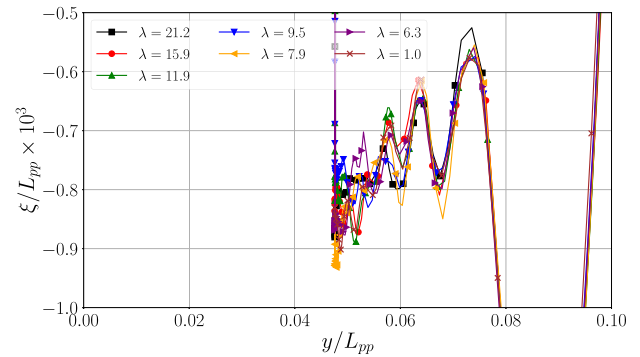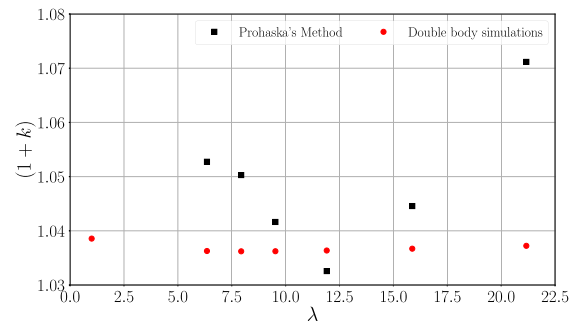
Prohaska's method is used to obtain $(1+k)$. It should also be mentioned that the results of the regression are strongly affected by the number of points used. On the other hand, the results from the double-body simulations result in a nearly constant form factor for this particular vessel, which is lower than that obtained from the experiments, with the exception of a single scale. One noteworthy aspect is that the largest change in the form factor in the double-body simulations is observed in the full-scale simulations, which could be due to the use of wall functions in that simulation.

The comparison of the scaled resistance coefficients with the full-scale measurements and simulations is depicted in Fig. 23. As a consequence of the nearly constant form factors obtained from the double-body simulations, the results of cases 2 and 3 are nearly identical, with the same being true for cases 4 and 5. As a consequence, the differences observed depend mainly on how the form factor was obtained, and on whether the wave resistance is estimated from the model-scale measurements or simulations, and for that reason we will restrict the discussion to cases 1, 2 and 4. When comparing cases 1 and 2, the difference lies in form factor, which was observed to be generally higher when it was obtained from the measurements. As a consequence, the estimated wave resistance is lower when Prohaska's method was used, resulting in lower full-scale resistance. Furthermore, the variation of the form factor observed in case 1 also causes a large change of the wave resistance with the scaling ratio. When considering case 4, the
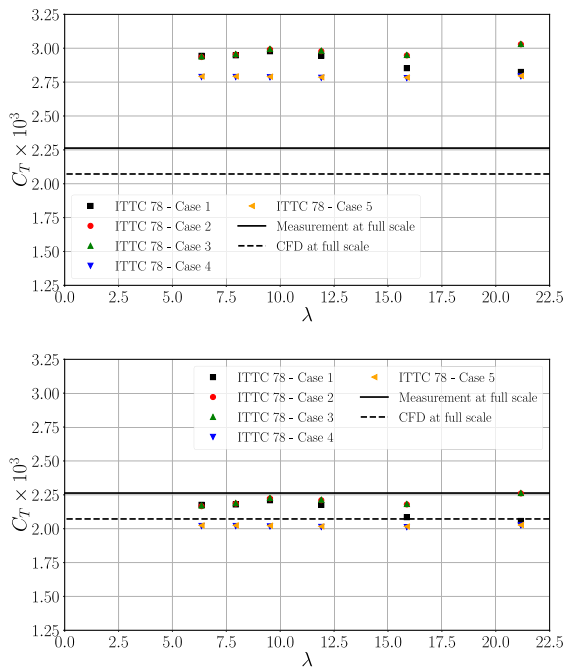
Fig. 23. Comparison of the scaled resistance coefficients obtained in the measurements and in the simulations with the full-scale resistance coefficient obtained in the experimental campaign and simulations, with different approaches to obtain the form factor according to the ITTC 1978 scaling procedure with (top) and without (bottom) roughness and air resistance effects.

variation of the wave resistance is much smaller, and so is the scaled resistance. When compared to the remaining cases, the estimation of the full-scale resistance is lower than the remaining approaches.

When the effects of roughness and air resistance are included in the ITTC 78 scaling procedure, the estimated full-scale resistance is much higher than the results obtained in the full-scale measurements or the full-scale simulations by around 32% and 35%, respectively. We also note that the difference between the full-scale results is much smaller than the effect of roughness in the scaling procedure, which leads to an increase to the resistance coefficient of around 6.8×10^{-4}. When the roughness and air resistance are excluded from the scaling procedure, the match with the full-scale results is improved. The results are particularly good for case 4, where only numerical data was used in the scaling procedure, showing good agreement with the results from the full-scale simulation and a relative difference of 2.6%. The results for case 1 now underpredict the resistance by 3.9%, although the comparison is not adequate since roughness effects are present in the measurements. The agreement for case 2 is better, with a difference of 2.8%, but the non-inclusion of roughness in the scaling procedure increases the uncertainty of the comparison.

5. Conclusions

This study addresses the prediction of the resistance for the Lucy Ashton, a paddle steamer which was used in an experimental campaign in the 1950s. This case corresponds to a unique set of data, as it is a full-scale resistance case, as jet engines were used for the propulsion of the ship, avoiding the use of a propeller and the need for a towing vessel which would cause interference effects. This ship geometry has not been used for any numerical work up until now, and with this work the authors hope to bring visibility to the measurements and establish its value and potential as a validation case.

Numerical simulations were carried out for the Lucy Ashton for a range of Froude numbers at full-scale, and for a constant Froude number with varying scaling ratios. Most of the simulations were

performed assuming the hull to be hydrodynamically smooth, and with no degrees of freedom on the ship. Nonetheless, the influence of roughness and of heave and pitch on the resistance coefficient were considered for a single condition at full-scale. The results were compared to available measurements tabulated in the original papers that describe the experiments.

The main outcomes of this work are as follows:

- The smearing of the free-surface on the surface of the hull was found to be problematic in all the simulations carried out, even at model-scale. This fact is likely related to the different strategies to handle the boundary layer, as it was resolved at model-scale and wall functions were used at full-scale. The smearing of the free surface results in an artificially lower resistance coefficient, due to the decrease viscosity in the smeared region. In order to handle this issue, a source term was used, which greatly remedies the situation, and was shown to have a negligible impact in a condition where the smearing of the free-surface was not significant.
- The simulations at full-scale and the comparison with the measurements showed the resistance coefficient to be underpredicted for all Froude numbers when surface roughness is not included and the ship is not free to heave and pitch. The inclusion of these effects lead to a much better agreement with the measured data, despite the uncertainty in the specification of the equivalent sand-grain roughness height. The comparison between the simulations performed with the double-body setup with those that included the free-surface displayed the limitations of the double-body approach as the Froude number increases and the wave making resistance becomes more important.
- The comparison performed at model-scale also showed the resistance coefficient obtained in the simulations to be significantly lower than that from the measurements. It is doubtful that surface roughness would play a part at model-scale, and the influence of laminar effects was not considered, as the measurements were carried out for conditions where the flow was tripped.
- The ITTC 78 scaling procedure was used to scale the model-scale data obtained in the measurements and in the simulations, and compare with the corresponding full-scale resistance. Using Prohaska's method to obtain the form factor was shown to lead to large variations with the scaling ratio, which are not present if the double-body simulations are used to obtain the form factor. An overprediction of the resistance coefficient was obtained when the scaling procedure was applied with the inclusion of roughness and air resistance. When the latter effects are not included, the application of the scaling procedure using the numerical model-scale data leads to a very good agreement with the full-scale CFD resistance.

CRediT authorship contribution statement

Rui Lopes: Writing – review & editing, Writing – original draft, Validation, Methodology, Investigation, Formal analysis, Conceptualization. **Arash Eslamdoost:** Writing – review & editing, Supervision, Resources, Methodology, Formal analysis, Conceptualization. **Rikard Johansson:** Writing – review & editing, Supervision, Conceptualization. **Seemontini RoyChoudhury:** Writing – review & editing, Supervision, Conceptualization. **Rickard E. Bensow:** Writing – review & editing, Supervision, Resources, Project administration, Methodology, Funding acquisition, Conceptualization. **Per Hogström:** Writing – review & editing, Resources, Conceptualization. **Dmitriy Ponkratov:** Writing – review & editing, Resources, Conceptualization.

Declaration of competing interest

The authors declare that they have no known competing financial interests or personal relationships that could have appeared to influence the work reported in this paper.

References

Castro, A.M., Carrica, P.M., Stern, F., 2011. Full scale self-propulsion computations using discretized propeller for the KRISO container ship KCS. Comput. & Fluids 51 (1), 35–47.

Conn, J.F.C., Lackenby, H., Walker, W.P., 1953. B.S.R.A. resistance experiments on the "Lucy Ashton". Part II - the ship-model correlation for the naked hull conditions. In: Proceedings of the Spring Meeting of the Institution of Naval Architects, London, United Kingdom.

Crichton, A.T., 1989. William and Robert Edmund Froude and the evolution of the ship-model experimental tank. Trans. Newcom. Soc. 61 (1), 33–49.

Demirel, Y.K., Turan, O., Incecik, A., 2017. Predicting the effect of biofouling on ship resistance using CFD. Appl. Ocean Res. 62, 100–118.

Denny, M.E., 1951. B.S.R.A. resistance experiments on the "Lucy Ashton". Part I - full-scale measurements. In: Proceedings of the International Conference of Naval Architects and Marine Engineers, London, United Kingdom.

Durbin, P., 1996. On the k-3 stagnation point anomaly. Int. J. Heat Fluid Flow 17 (1), 89–90.

Eça, L., Hoekstra, M., 2014. A procedure for the estimation of the numerical uncertainty of CFD calculations based on grid refinement studies. J. Comput. Phys. 262, 104–130.

García-Gómez, A., 2000. On the form factor scale effect. Ocean Eng. 27 (1), 97–109.

Granville, P.S., 1974. A modified Froude method for determining full-scale resistance of surface ships from towed models. J. Ship Res. 18 (04), 215–223.

Gray-Stephens, A., Tezdogan, T., Day, S., 2021. Minimizing numerical ventilation in computational fluid dynamics simulations of high-speed planning hulls. J. Offshore Mech. Arct. Eng. 143 (3), 031903.

Hirt, C.W., Nichols, B.D., 1981. Volume of fluid (VOF) method for the dynamics of free boundaries. J. Comput. Phys. 39 (1), 201–225.

Huang, L., Pena, B., Thomas, G., 2023. Towards a full-scale CFD guideline for simulating a ship advancing in open water. Ship Technol. Res. 1–17.

ITTC, 1999. The propulsion committee: final report and recommendations to the 22nd ITTC. In: Proceedings of the 22nd ITTC, Seoul/Shanghai, South Korea/China.

ITTC, 2008. The specialist committee on powering performance prediction: final report and recommendations to the 25th ITTC. In: Proceedings of the 25th ITTC, Fukuoka, Japan.

ITTC, 2021. 1978 ITTC Performance Prediction Method. ITTC - Quality System Manual Recommended Procedures and Guidelines 7.5-02-03-01.4.

Jasak, H., Vukčević, V., Gatin, I., Lalović, I., 2019. CFD validation and grid sensitivity studies of full scale ship self propulsion. Int. J. Nav. Archit. Ocean. Eng. 11 (1), 33–43.

Joubert, P.N., Matheson, N., 1970. Wind tunnel tests of two Lucy Ashton reflex geosims. J. Ship Res. 14 (04), 241–276.

Korkmaz, K.B., Werner, S., Bensow, R., 2021a. Verification and validation of CFD based form factors as a combined CFD/EFD method. J. Mar. Sci. Eng. 9 (1), 75.

Korkmaz, K.B., Werner, S., Sakamoto, N., Queutey, P., Deng, G., Yuling, G., Guoxiang, D., Maki, K., Ye, H., Akinturk, A., et al., 2021b. CFD based form factor determination method. Ocean Eng. 220, 108451.

Lackenby, H., 1954. B.S.R.A. resistance experiments on the "Lucy Ashton". Part III - the ship-model correlation for the shaft-appendage conditions. In: Proceedings of the Autumn Meeting of the Institution of Naval Architects, Torquay, United Kingdom.

Liu, L., Chen, M., Yu, J., Zhang, Z., Wang, X., 2021. Full-scale simulation of self-propulsion for a free-running submarine. Phys. Fluids 33 (4).

Menter, F.R., 1994. Two-Equation Eddy-Viscosity Turbulence Models for Engineering Applications. AIAA J. 32 (8), 1598–1605.

Mikkelsen, H., Walther, J.H., 2020. Effect of roughness in full-scale validation of a CFD model of self-propelled ships. Appl. Ocean Res. 99, 102162.

Muzaferija, S., Peric, M., 1998. Computation of free surface flows using interface-tracking and interface-capturing methods. In: Nonlinear Water-Wave Interaction. Computational Mechanics Publications.

Niklas, K., Pruszko, H., 2019. Full-scale CFD simulations for the determination of ship resistance as a rational, alternative method to towing tank experiments. Ocean Eng. 190, 106435.

Ponkratov, D., 2017. Lloyd's Register's Full-Scale Numerical Modelling Workshop.

Ponkratov, D., Zegos, C., 2015. Validation of ship scale CFD self-propulsion simulation by direct comparison with sea trials results. In: Proceedings of the Fourth International Symposium on Marine Propulsors, Austin, Texas, USA.

Quist, N.A., Christensen, R.H., Mikkelsen, H., Walther, J.H., 2023. Validation of a full scale CFD simulation of a self-propelled ship with measured hull roughness and effect of welding seams on hull resistance. Appl. Ocean Res. 141, 103746.

Sezen, S., Delen, C., Dogrul, A., Atlar, M., 2021. An investigation of scale effects on the self-propulsion characteristics of a submarine. Appl. Ocean Res. 113, 102728.

Smith, S.L., 1955. B.S.R.A. resistance experiments on the "Lucy Ashton". Part IV - miscellaneous investigations and general appraisal. In: Proceedings of the Spring Meeting of the Institution of Naval Architects, London, United Kingdom.

Smits, A., 1982. Turbulence stimulation and the initial boundary-layer development on two ship forms. J. Ship Res. 26 (03), 166–175.

Smits, A., Matheson, N., Joubert, P., 1980. Some experiments on artificially roughened Lucy Ashton geosims. J. Ship Res. 24 (03), 170–180.

Song, K., Guo, C., Sun, C., Wang, C., Gong, J., Li, P., Wang, L., 2021. Simulation strategy of the full-scale ship resistance and propulsion performance. Eng. Appl. Comput. Fluid Mech. 15 (1), 1321–1342.

Terziev, M., Tezdogan, T., Incecik, A., 2019. A geosim analysis of ship resistance decomposition and scale effects with the aid of CFD. Appl. Ocean Res. 92, 101930.

Viola, I.M., Flay, R., Ponzini, R., 2012. CFD analysis of the hydrodynamic performance of two candidate america's cup AC33 hulls. Trans. R. Inst. Nav. Archit. Part B: Int. J. Small Craft Technol. 154 (1), B1–B12.